

Femtosecond versus picosecond all-optical switching of Si woodpile photonic crystals

Philip J. Harding,^{1,2} Tijmen G. Euser,^{1,3} and Willem L. Vos^{1,2}

¹*Center for Nanophotonics, FOM Institute for Atomic and Molecular Physics (AMOLF),*

Kruislaan 407, 1098 SJ Amsterdam, The Netherlands

²*Complex Photonic Systems (COPS),*

MESA+ Institute for Nanotechnology,

University of Twente, 7500 AE Enschede, The Netherlands

³*Currently with Max-Planck Research Group (IOIP), University of Erlangen-Nuremberg,*

Günther-Scharowsky-Str. 1/Bau 24, 91058 Erlangen, Germany

Abstract

We present a systematic study of ultrafast all-optical switching of Si woodpile crystals using broadband tunable nondegenerate pump-probe spectroscopy. Tuning the pump frequency through half the electronic bandgap of Si, we observe that the broadband spectral properties of the crystal's stopgap at probe delays of 1 ps behave in accordance with a Drude description of free carriers. Within 100 fs of the pump-probe coincidence however, two contributions to the stopgap's spectral properties are identified: the optical Kerr effect, and nondegenerate two-photon absorption. Since the latter has been hitherto disregarded in ultrafast photonic switching, we especially emphasize this contribution by generalizing the usual nonlinear figure of merit to a nondegenerate figure of merit (NFOM). Using this NFOM, which is valid for *all* optical switching processes, we can identify pump and probe parameter space for which instantaneous switching maximizes the Kerr coefficient while limiting both pump and probe absorption.

I. INTRODUCTION

The interest to optically switch photonic structures has recently gathered momentum due to the inherent fastness of the process. While the switching speed of conventional transistors is ultimately limited by heat dissipation, no such limitation is known for optical systems in the absence of absorption. To date, the dispersion of photo-induced free carriers is widely exploited to induce ultrafast changes in the photonic structure's optical properties. Then, propagation switching, optical modulation, trapping and releasing photons, frequency- and bandwidth conversion, and even ultrafast switching of the density of states are possible^{1,2,3,4,5,6}.

Free carrier switching has many advantages to other sorts of switching. First, the carriers are generated within ps, allowing for potentially high repetition rates⁷. Indeed, currently many efforts are devoted to decreasing the timescales of switching in polycrystalline silicon, achievable through implanting additional recombination centers such as ions^{8,9,10}. In contrast, molecular reorientation in liquid crystals responsible for changes in refractive indices gives rise to timescales of three to six orders of magnitude slower^{11,12,13}, rendering them useless in ultrafast devices. Thermal and mechanical tuning suffer the same fate^{14,15}. Second, free carriers can be generated all-optically, the generation therefore being possible by on-chip diode lasers. Third, the change can scale linearly or quadratically with intensity, depending on the relative frequency of the pump pulse to the switched semiconductor. Therefore, large dynamic ranges can be achieved with only small intensity changes. Finally, the induced refractive index change is large compared other techniques. To compare, the only other switching technique of comparable speed is the optical Kerr effect, which has nonlinear coefficients orders magnitude lower^{16,17,18}.

Recently, several groups^{19,20,21} have claimed to have experimental evidence of this Kerr nonlinearity in photonic crystals.⁴⁸ The reasoning in all cases is the instantaneous nature of the effect, with a decrease in reflectivity or transmission coinciding with the cross-correlation of the pump and probe pulses. The duration of the pump and probe pulses is then the limitation to potential repetition rates, instead of the recombination times of the free carriers. Kerr switching could increase the repetition rate from GHz to THz. Here, we critically evaluate optical processes at both instantaneous (fs) as well as ps timescales. At coincidence, we will show that two competing processes change the optical properties as witnessed from

reflectivity measurements. From these two processes, we propose a general nondegenerate figure of merit (NFOM), which has wide implications for all-optical fs switching, extending to DOS switching and ultimately to the dynamic control of spontaneous emission.

II. EXPERIMENTAL SETUP AND SAMPLE

Our setup consists of a regeneratively amplified Ti:Sapph laser (Spectra Physics Hurricane) which drives two independently tunable optical parametric amplifiers (OPAs, Topas). The OPAs have a continuously tunable output frequency between 0.44 and 2.4 eV, with nearly bandwidth limited pulses (relative width of 1.33%, bandwidth limited equivalent to $\tau_P = 110$ fs) with pulse durations of $\tau_P = 140 \pm 10$ fs (measured at $E_{\text{Pump}} = 0.95$ eV) and a pulse energy of at least 20 μJ . The probe beam is normally incident $\theta = 0^\circ$ on the sample, and is focused to a Gaussian spot of 32 μm FWHM (at $E_{\text{probe}} = 1.24$ eV) at a small angular divergence $\text{NA} = 0.02$. The reflectivity was calibrated by referencing to a gold mirror. A versatile measurement scheme was developed to subtract the pump background from the probe signal, and to compensate for possible pulse-to-pulse variations in the output of our laser^{23,25}.

Figure 1 shows a high resolution scanning electron micrograph of the photonic woodpile structure made by Jim Fleming at Sandia National Laboratories²⁶. It consists of 5 layers of polysilicon (p-Si) rods ($n' = 3.45$) stacked orthogonally upon one another, the n -th layer shifted by half an interrod distance with respect to the $(n+2)$ th layer. This structure gives rise to a diamond lattice, for which a first-order band gap is predicted²⁷. The dimensions of the rods were chosen so as to aim the center the band gap around telecom frequencies ($E_{\text{Tele}} = 0.735$ eV). The E-field of the probe beam is polarized along the $[\bar{1}10]$ direction of the crystal, that is, perpendicular to the first row of rods. The last row of rods is supported by a 70 nm thick SiN layer of refractive index ≈ 2 . At our probe frequencies the SiN layer is optically thin, and is not expected to influence reflectivity measurements.

The sample has been characterized extensively elsewhere^{25,28}. Over the sample, the mutual alignment of the rods differs. These differences are spatially separated, and allow the sample to be divided into 16 domains, which we denote by A1 through D4 in analogy to a chessboard. Here, we perform measurements on both A1 and D4, and are thus able to validate our results for different sample conditions. The symmetry of D4 is face centered

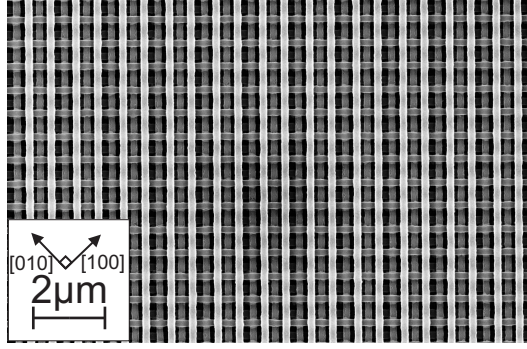


FIG. 1: High resolution scanning electron micrograph of the surface normal to $[001]$ of a Si woodpile crystal at domain D4. The width and thickness of each rod is $175 \pm 10\text{nm}$ and $155 \pm 10\text{nm}$, respectively.

orthorhombic, while A1 is body centered orthorhombic.

III. LINEAR REFLECTIVITY

Figure 2 shows a linear reflectivity spectrum of the woodpile photonic crystal. The high peak centered at $E_0 = 0.9\text{ eV}$ corresponds to the $\Gamma - X$ stop gap in the band structure, which is part of the 3D photonic band gap of Si woodpile photonic crystals^{23,29,30}. The maximum reflectivity of $95 \pm 2\%$ and the broad width of $\Delta E = 0.46\text{ eV}$ FWHM (full width at half maximum) confirm the strong interaction of the crystal with light³¹. We note that the large relative width of $S = 47\%$ is the largest measured for any photonic crystal so far.

We can associate a length scale with the the spectral width of the stopband. The Bragg length L_B is the length at which the incoming intensity has dropped to $1/e$ of its initial value, and is given by³²

$$L_B = \frac{\lambda}{\pi S}, \quad (1)$$

where λ is the center wavelength of the stopgap. We deduce a Bragg length of $L_B = 950\text{ nm}$, corresponding to 1.2 unit cells. In contrast, other 3D structures with a lower photonic strength have much higher L_B : TiO_2 inverse opals, for example, have $L_B \approx 4\text{ }\mu\text{m}$, while polystyrene opals have $L_B \approx 8\text{ }\mu\text{m}$ and SiO_2 opals $L_B \approx 9\text{ }\mu\text{m}$ estimated from the bandstructure³².

The high photonic strength also causes the steep edges of the peak, which we will in

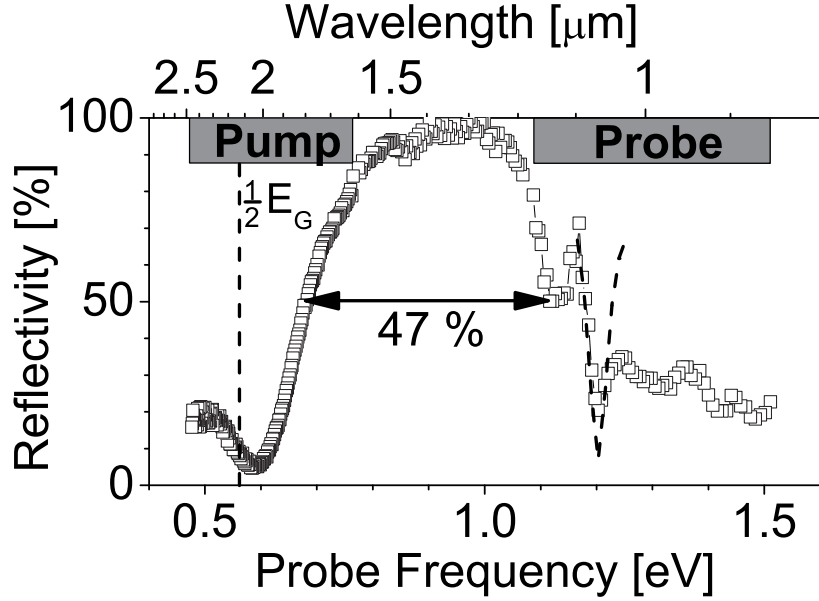


FIG. 2: Linear reflectivity spectrum of the woodpile photonic crystal measured normal to the [001] direction at a sample domain D4 shown in figure 1. The E-field is perpendicular to the first row of rods. A stopgap near 0.9 eV gives rise to a high maximum reflectivity of $95 \pm 2\%$ and has a broad relative width of 47%, indicating a high photonic strength. At high frequencies > 1.2 eV, the spectral features are attributed to Fabry-Pérot-type fringes. The pump frequencies (shaded box) were tuned at the red edge through half the electronic band gap $E_G = 1.12$ eV of silicon (vertical dashed line), and the probe frequencies at the blue edge of the stopband. The dashed curve is a calculation with the Scalar Wave Approximation in the region of interest.

first instance probe at the blue edge of the stopband. At these frequencies, all induced changes in optical properties of the Si backbone will show a large change in reflectivity, important for switching applications. The probe frequencies (indicated by the shaded box) span both the blue edge of the stopband as well as the fringes. These have been assigned to Fabry-Pérot-type interferences³³, but the reflectivity spectrum of woodpiles is still subject to debate^{25,28}.

IV. SWITCHED REFLECTIVITY VS. TIME AT ONE PROBE FREQUENCY

The pump frequencies E_{Pump} were chosen as to tune through half the electronic band gap of silicon, where the gap is $E_G = 1.12$ eV. Both the Kerr coefficient n_2 as the degenerate two-photon absorption coefficient β_{11} have recently been shown to vary strongly in the vicinity of $\frac{1}{2}E_G$ ^{16,17,18,34,35,36}.

On domain A1 we measured differential reflectivity $\Delta R/R$ vs. probe delay Δt as a function of E_{Pump} (figure 3). At this sample position, the probe frequency of $E_{\text{Probe}} = 1.13$ eV corresponds to the foot of the blue stopband edge. At positive probe delays $\Delta t = 1$ ps and at pump frequencies $E_{\text{Pump}} > \frac{1}{2}E_G = 0.56$ eV, we observe a large positive differential reflectivity $(\Delta R/R)_{\text{FC}}$ due to a blueshift of the photonic features. This shift is caused by a decrease of the refractive index of the p-Si backbone that agrees well with a Drude description of the excited free carriers²³. When E_{Pump} is reduced to below $\frac{1}{2}E_G$, the dispersion vanishes, since no free carriers are excited by a two-photon process.

Near coincidence, at $\Delta t = 0$ ps, we observe a trough of magnitude $(\Delta R/R)_{\text{coinc}}$. The width of this trough varies between 240 fs ($E_{\text{Pump}} = 0.52$ eV) and 160 fs ($E_{\text{Pump}} = 0.62$ eV). The expected cross-correlation duration for two pulses of $\tau_P = 140 \pm 10$ fs is $\tau_P \times \sqrt{2} = 198$ fs, in reasonable agreement with the measured values. The variation with pump frequency is partially related to the shorter pulse duration at higher frequencies which corresponds to a wider spectral width of the pulse. As E_{Pump} increases to above $\frac{1}{2}E_G$, the magnitude of $(\Delta R/R)_{\text{coinc}}$ grows until it saturates at $E_{\text{Pump}} = 0.62$ eV, just over $\frac{1}{2}E_G$.

V. SWITCHED REFLECTIVITY VS. FREQUENCY

A. Reflectivity vs. frequency at coincidence

In order to investigate the precise nature of $(\Delta R/R)_{\text{coinc}}$, we have measured the differential reflectivity at coincidence on domain D4 for a wide range of probe frequencies, which we plot in figure 4(c). We make two important observations. Firstly, with increasing E_{Pump} , the variation in the data becomes stronger. The differential reflectivity becomes increasingly negative with both increasing pump and increasing probe frequency. These negative values indicate optical absorption. Secondly, at 1.22 eV, a peak appears in the differential reflectivity that corresponds to a red edge in the linear reflectivity (figure 4(a)); likewise, a

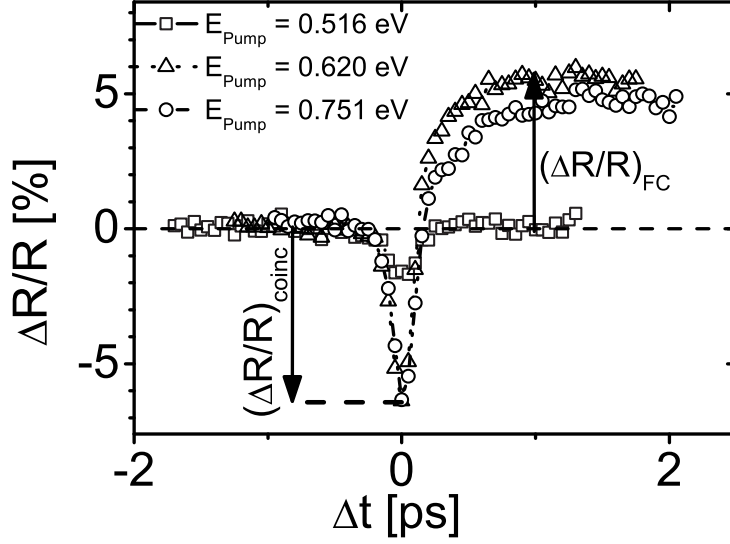


FIG. 3: Differential reflectivity $\Delta R/R$ versus probe delay Δt taken at different pump frequencies E_{Pump} and at probe frequency $E_{\text{Probe}} = 1.13$ eV, sample domain A1. At $\Delta t = 0$ ps, the pump and probe are coincident, and the differential reflectivity $(\Delta R/R)_{\text{coinc}}$ decreases. At $\Delta t = 1$ ps, the differential reflectivity $(\Delta R/R)_{\text{FC}}$ has increased due to the dispersion of the free carriers (FC). The peak pump intensity varies between $I_{\text{Pump}} = 10 \pm 1 \text{ GWcm}^{-2}$ ($E_{\text{Pump}} = 0.516$ eV) and $I_{\text{Pump}} = 25 \pm 2 \text{ GWcm}^{-2}$ ($E_{\text{Pump}} = 0.75$ eV), and the probe intensity was $I_{\text{Probe}} = 3 \pm 2 \text{ GWcm}^{-2}$.

trough appears at 1.18 eV which corresponds to a blue edge. This clear dispersive change is indicative of a redshift of the photonic features. Thus, we conclude that, when pump and probe are coincident, two effects contribute to the differential reflectivity signal: Nonlinear dispersion, which we attribute to the optical Kerr effect, and absorption. This absorption is seen to increase for an increase of either pump or probe frequencies. Since in addition the sum of pump and probe frequencies exceeds the absorption edge of p-Si, we conclude that the negative differential reflectivity is due to an instantaneous nondegenerate two photon process. Recent work^{19,20,21} has attributed the behavior at coincidence to the Kerr effect, due to the lack of dispersive data. We for the first time identify the different contributions at coincidence. Before quantifying the two different contributions from the data, we will first briefly describe the measured effects of the free carriers on the spectral properties.

B. Reflectivity vs. frequency at $\Delta t = 1$ ps

Figure 4(b) shows the differential reflectivity at one positive probe delay of $\Delta t = 1$ ps that is caused by free carriers. Because the data varies around 0, we conclude that the induced absorption is minimal. The peak at 1.2 eV corresponds to the blue edge of the linear reflectivity peak at 1.175 eV, the two troughs at 1.23 eV and 1.16 eV corresponds to the red edges of the reflectivity peaks at 1.175 and 1.25 eV, respectively. Therefore, the data is consistent with a blueshift, or a decrease of the refractive index $\Delta n'$ as a result of the free carriers.

C. Model: The Extended Scalar Wave Approximation

To quantify the free carrier effects as well as the two nonlinear contributions at coincidence, a model of the woodpile's linear and nonlinear spectral properties is necessary. In this section, we explain the principle behind the model, and delineate it against others.

The optical properties of real woodpile photonic crystals have previously been calculated with an exact modal method (EMM)²⁹. For each layer in z , the dielectric constant $\epsilon(\mathbf{r})$ is expanded in Fourier series in x and y , perpendicular to z . The electric and magnetic fields can be calculated from the vector wave equation. The solutions are then subject to boundary conditions from the solutions in adjacent layers. In that way, the fields in the complete structure can be calculated. It is different to a bandstructure calculation in that the structure is finite in one direction. From the boundary conditions at the first and the last layer, it is possible to calculate the reflectivity. The EMM has been shown to agree reasonably well to reflectivity measurements at frequencies up to the stopgap^{23,25,33}, but fails to reproduce measurements at the blue edge of the stopgap. If we quantitatively want to understand the magnitude of the induced changes, it is important for any model to correctly reproduce the linear reflectivity first.

Here, we will employ the Scalar Wave Approximation (SWA) to calculate the reflectivity. The dielectric function in beam direction $\epsilon(z)$ and the lattice spacing can be written in terms of their Fourier components U_G and G , respectively. For binary structures composed of materials of two different dielectric constants, it can be shown that³²

$$U_G = \Delta\epsilon f_G, G \neq 0, \quad (2)$$

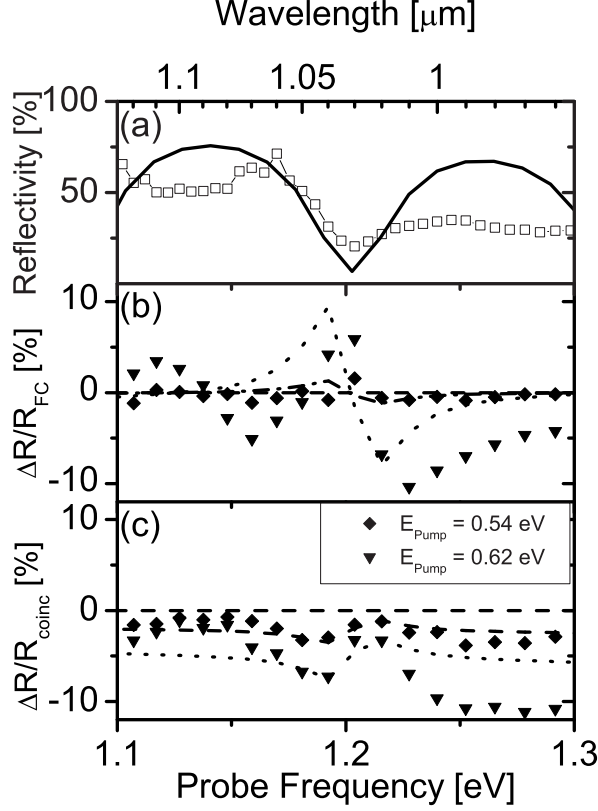


FIG. 4: (a): Measured linear reflectivity versus probe frequency (squares) on domain D4 compared to a scalar two-band model (solid curve). (b) The differential reflectivity at delay $\Delta t = 1$ ps caused by the free carriers $(\Delta R/R)_{\text{FC}}$ shows mostly dispersive features, as seen from the symmetric variation of $\Delta R/R$ around 0. When increasing the pump frequency from 0.54 (solid triangles) to 0.62 eV (open triangles), these dispersive features increase in magnitude. (c): At $\Delta t = 0$ ps, dispersive as well as absorptive elements can be observed in $\Delta R/R_{\text{coinc}}$, increasingly so when increasing the pump frequency from $E_{\text{Pump}} = 0.54$ eV to $E_{\text{Pump}} = 0.62$ eV. Dashed and dotted curves correspond to the fits of the extended SWA at $E_{\text{Pump}} = 0.54$ and 0.62 eV, respectively. The pump intensity was $I_{\text{Pump}} = 36 \pm 4 \text{ GWcm}^{-2}$ ($E_{\text{Pump}} = 0.54$ eV) and $I_{\text{Pump}} = 46 \pm 5 \text{ GWcm}^{-2}$ ($E_{\text{Pump}} = 0.62$ eV).

where $\Delta\epsilon$ is the difference of the dielectric constants, and f_G is the Fourier Transform of the indicator function $f(z)$, where $\epsilon(z) = \epsilon_1 + \Delta\epsilon f(z)$. From a change in $\Delta\epsilon$, a new U_G can readily be obtained. The electric field *in* the crystal can now be calculated by considering only the first two bands, k (incident) and $k - G$ (Bragg diffracted). Outside the crystal,

the field can be determined from the two boundary conditions the two bands are subject to. Thus, the transmission and reflectivity can be determined.

Two remarks are at order: a. Despite evidence of polarization effects on the reflectivity³³, the scalar wave approximation inherently cannot take polarization into account. However, since the incident polarization does not change during the experiment, the induced change in reflectivity can just as well be modelled with a scalar equation. b. While EMM can correctly include absorption by solving Maxwell's equations with a complex ϵ in any one layer, the SWA uses an approximated two-band bandstructure, for which modes can only exist in the absence of extinction. To nevertheless include absorption, the reflectivity was reduced by a factor $\exp(-2L/\ell_{\text{abs}})$, where $\ell_{\text{abs}} = 1/(2\phi n'' n' k)$, and ϕ is the filling fraction of the Si (26%). The factor of 2 in the exponent accounts for the beam passing through the sample twice. This results in the magnitude of the reflectivity over all the spectrum to decrease, while induced absorption normally causes the visibility to decrease, due to the increasing breakdown in interference. This second point forces us to view the fitted values of n' and n'' as qualitative.

We fit the linear reflectivity obtained by the scalar wave approximation to the region given in fig. 4(a). The best agreement to the measured reflectivity is obtained with $G = 2\pi/(393 \text{ nm})$ and $U_G = -0.8$. Due to the scalar nature of the model, we expect no correlation between the real and fitted lattice constants. In the model, we included the dispersion and absorption of p-Si (from³⁷, see fig. 5), and have taken bulk Si as the substrate, neglecting the optically thin layer of SiN ($n' = 2, d = 70\text{nm}$). Since the optical features in the reflectivity spectrum are much broader than the probe bandwidth, no convolution of the calculated spectrum with the probe is necessary.

D. Interpretation of spectra at coincidence

We match the calculated dispersive differential reflectivity to the strong signature of a redshift at $E_{\text{Probe}} = 1.2 \text{ eV}$ by fitting two independent parameters $\Delta n' = n_2 I_{\text{Pump}}$ and n'' over the range $1.18 \text{ eV} < E_{\text{Probe}} < 1.23 \text{ eV}$ by minimizing the least squares. The differential reflectivity was obtained as follows: using the G obtained previously from the fit to the linear spectrum, the U_G was changed via the changed $\Delta\epsilon$ (equation 2), and the switched reflectivity spectrum was calculated from the new U_G . Error margins for the parameters

were taken as the values at which the least squares values had changed by 10%.

Figure 4(c) shows the fits to two spectra obtained at two different E_{Pump} . The remarkable agreement of this approximate model with the data confirms that the subtle interplay of nonlinear dispersion as well as nondegenerate absorption leads to the observed features. At frequencies lower than 1.2 eV, the fitted curves tend to be lower than the measurements. Also, to the blue of 1.2 eV, the calculated differential reflectivity is mostly higher than the measurements. These deviations are due to our fit not taking into account the nondegenerate nature of β_{12} , but setting it to one value for all probe frequencies.

Figure 5(a) and (b) shows the absorptive and dispersive part of the induced refractive index at coincidence, respectively, as returned from the fits. The value at $E_{\text{Pump}} = 0.7$ eV is excluded due to experimental artifact in that measurement. Figure 5(a) shows that the imaginary refractive index n'' increases for pump frequencies $E_{\text{Pump}} > 0.55$ eV. Since we are working at pump-probe coincidence, those frequencies correspond to a sum of pump and probe frequencies $E_{\text{Pump}} + E_{\text{Probe}} > 1.75$ eV. Since these values are larger than the optical gap of p-Si of $1.4 \text{ eV} < E_{\text{opt}} < 1.6 \text{ eV}$, depending on the degree of polycrystallinity³⁸, it is clear that the simultaneous presence of pump and probe photons induces optical absorption. From recent calculations³⁹, the N_{ph} -photon process in a direct transition can be viewed as a single-photon process with an energy gap rescaled to E_G/N_{ph} , where N_{ph} is the number of photons. In other words, $(E_{\text{Pump}} + E_{\text{Probe}})/2 = E'$ in the present two beam case, where E' is a rescaled energy. Therefore, we can compare the *shape* of our extracted nondegenerate absorption coefficient to the linear absorption. We therefore also plot the linear absorption of p-Si (Low Pressure Chemical Vapor Deposition, processing temperature 545°C) similar to that used to make the woodpile crystals³⁷. The behavior of the linear absorption agrees reasonably with that of the nondegenerate absorption, supporting calculations from³⁹. For our intensities, the nondegenerate absorption remains significantly below the linear absorption. Pumping and/or probing at higher frequencies causes the absorption to increase, as do higher *pump* intensities.

Higher *probe* intensities do not influence the magnitude of the nondegenerate absorption: in the absence of linear absorption, as in our case, the differential equation governing nondegenerate two photon absorption is⁴⁰

$$\frac{dI_{\text{Probe}}}{dz} = -2\beta_{12}(E_{\text{Probe}}, E_{\text{Pump}})I_{\text{Pump}}I_{\text{Probe}}(z) \quad (3)$$

The nondegenerate two-photon absorption coefficient β_{12} is related to n'' as $\beta_{12}I_{\text{Pump}} = 2n''n'/k$. From equation 3 we see that higher probe intensities do not increase absorption: The coefficient of $-I_{\text{Probe}}(z)$ is $2\beta_{12}(E_{\text{Probe}} + E_{\text{Pump}})I_{\text{Pump}} = \alpha_{\text{eff}}$, an effective absorption coefficient. Higher probe intensities merely lead to a higher *absorbance*, commensurate to the number of absorbed photons.

The real part of the instantaneous change in n is plotted in figure 5(b). At low pump frequencies of 0.52 eV, the change is 0.5×10^{-3} , while it more than doubles at $E_{\text{Pump}} = 0.56$ eV. At $E_{\text{Pump}} = 0.62$ eV, $\Delta n'$ increases only marginally. We compare our measurements to other recent degenerate measurements of the nonlinear dispersion of bulk Si^{16,17,18}. In order to be able to make the comparison, we made use of the rescaling condition. We find excellent agreement to the latter, but surprisingly the measurements of¹⁷ are an order of magnitude higher, despite being measured with the same z-scan technique as^{16,18}. We also compare our measured data to a relation for n_2 derived for direct-gap semiconductors⁴¹ multiplied by our pump intensity I_{Pump} . The functional form agrees well with our data. At higher probe frequencies, the theoretical relation differs from the data of^{16,18}. A theory able to calculate the degenerate nonlinear properties of an indirect semiconductor such as silicon was recently proposed³⁹ and was shown to agree well with degenerate nonlinearities using the rescaling condition¹⁷.

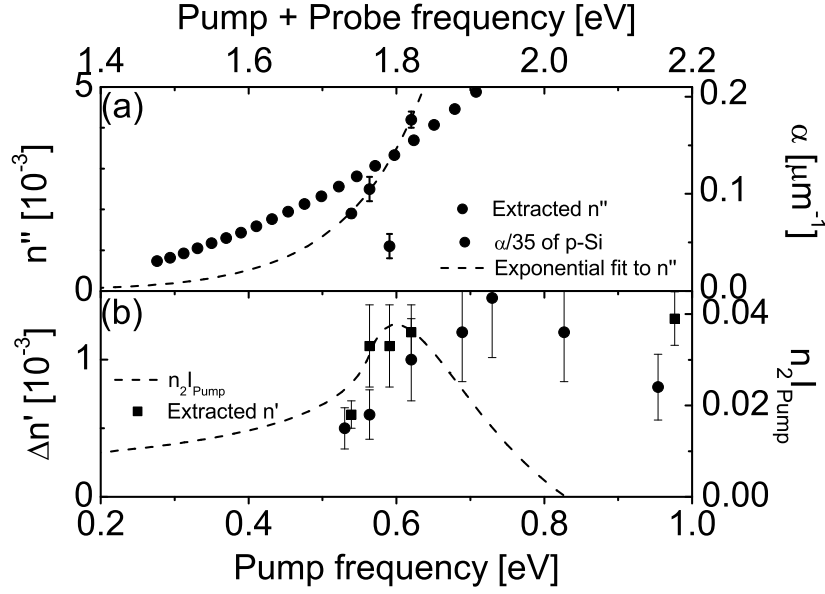


FIG. 5: (a): Imaginary refractive index (n'' , solid circles) vs. pump frequency E_{Pump} (lower axis) obtained by modeling our data (fig. 4) and upper abscissa is the sum of the pump and probe frequencies E_{Total} . The right scale shows the corresponding absorption coefficient. To compare to our effective α , we plot the scaled absorption coefficient for Low Pressure Chemical Vapor Deposition p-Si (open circles) annealed at 545°C , similar to the backbone of our woodpile crystals. (b): Change in real refractive index $\Delta n'$ (left scale, solid squares) vs. pump frequency E_{Pump} from our nondegenerate measurements. We plot other recent degenerate measurements for comparison: Open squares from¹⁶ and open circles from¹⁸. Data from¹⁷ exceeds the scale by one order of magnitude. The theoretical relation predicted by⁴¹ is also shown (dashed curve, right scale).

E. Interpretation of ps switching

Using the same two-band model from section V C, we can also interpret the picosecond free carrier behavior. Therefore, the calculated differential reflectivity can be fitted to $(\Delta R/R)_{\text{FC}}$ by calculating the complex refractive index change according to the Drude model (figure 4(b)). The carrier density N is given by

$$N = \frac{I_{\text{Pump}}^2 \tau_P \beta_{11}}{2E_{\text{Pump}} e}, \quad (4)$$

where β_{11} is the degenerate two photon absorption coefficient. At our pump frequencies, we can neglect absorption. For carrier densities $N < 10^{28} \text{ m}^{-3}$, well above densities created in our experiments, the change in dielectric constant is⁴²

$$\epsilon_{\text{fc}} = - \left(\frac{\omega_P}{\omega} \right)^2 (1 - i(\omega\tau_D)^{-1}), \quad (5)$$

where $\omega_P^2 = Ne^2/(m^*\epsilon_0)$ is the plasma frequency squared in $(\text{rad/s})^2$ and e and m^* are the charge and effective optical mass of the carriers, and ω the probe frequency in rad/s . Equation 5 is valid for $(\omega\tau_D)^{-1} \ll 1$, which is the case for our probe frequencies and damping times. For a given I_{Pump} therefore, we can fit the differential reflectivity resulting from a changing β_{11} to $(\Delta R/R)_{\text{FC}}$.

The β_{11} vs. E_{Pump} as returned from the fits is plotted in figure 6. For $E_{\text{Pump}} < \frac{1}{2}E_G$, β_{11} tends to 0, as expected. Increasing E_{Pump} to above 0.54 eV, there is a marked increase. At $E_{\text{Pump}} = 0.62 \text{ eV}$, β_{11} has increased to as much as $5 \pm 1 \text{ cmGW}^{-1}$. This value is considerably higher than other published values: In the same plot, values are compared to^{16,17,18}, measured with the same z-scan technique²⁴ on crystalline Si. For our sample however, values as high as $\beta_{11} = 60 \pm 15 \text{ cmGW}^{-1}$ have been reported²⁵. Amorphous Si (a-Si) formed by Chemical Vapor Deposition has very recently been shown to possess a higher nonlinearity than crystalline Si (c-Si)⁴³.

We are now able to calculate some crucial parameters to characterize the quality of the switching process. We find that the carrier induced absorption length is $\ell_{\text{abs}} = 123 \pm 50 \text{ }\mu\text{m}$, much longer than L_B , confirming that the absorption is negligible indeed. The pump homogeneity length, another important parameter describing the spatial homogeneity of carriers, is $\ell_{\text{hom}} = (I_{\text{Pump}}\beta_{11})^{-1} = 44 \pm 10 \text{ }\mu\text{m}$, or $170 \pm 40 L_B$ at $E_{\text{Pump}} = 0.62 \text{ eV}$ and $I_{\text{Pump}} = 46 \pm 5 \text{ GWcm}^{-2}$. This calculation highlights the advantage of two-photon absorption³⁴ to

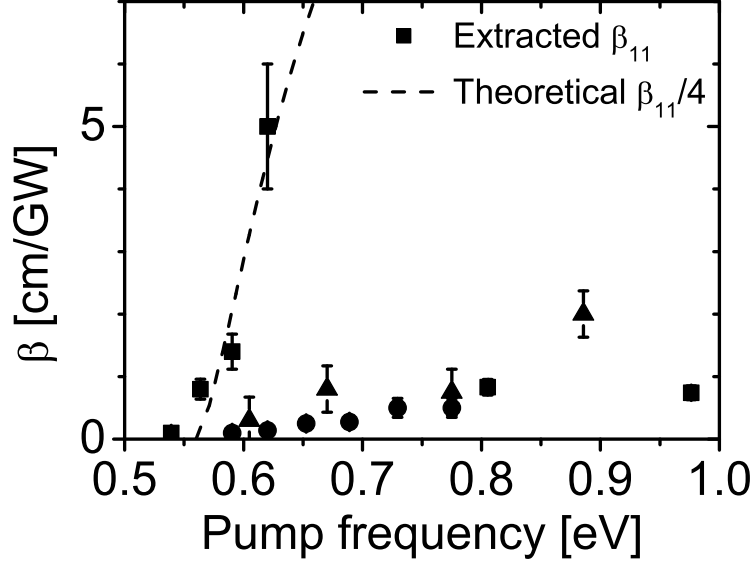


FIG. 6: β_{11} vs. pump frequency (solid squares). We fit the differential reflectivity obtained from the two-band model to the data with β_{11} as the only free parameter. Other data are from¹⁶ (open squares),¹⁸ (open circles), and¹⁷ (triangles).

one-photon absorption in which absorption limits the pump homogeneity^{14,20,21}. To compare, the absorption length of the nondegenerate two-photon process is $\approx 10 \mu\text{m}$. We conclude that for our switching conditions, both the pump and the probe absorption length remain well above L , and that thus instantaneous switching yields favorable conditions for our pump and probe frequencies, and pump intensities.

F. Reflectivity vs. pump frequency at coincidence

Having analyzed spectra of the reflectivity at coincidence and at $\Delta t = 1 \text{ ps}$, we return to figure 3. Experimental conditions had prevented us from taking more than 4 probe frequency- and time-resolved spectra, mostly related to the long measurement times. Having identified two competing processes at coincidence, we can now focus on time-resolved spectra which depend on pump frequency only. Figure 7 shows $(\Delta R/R)_{\text{coinc}}$ as a function of E_{Pump} . Here, I_{Pump} has been corrected for three important pump beam parameters: i.,

the increase in intensity with increasing E_{Pump} because of the decreasing Gaussian focus;⁴⁹ ii. the change in pump intensity due to the frequency dependent reflectivity of the pump, see figure 2; and iii. the measured 10% change in pump power over the frequency range of the OPA. For i., $(\Delta R/R)_{\text{coinc}}$ is assumed to vary quadratically with E_{Pump} , assuming that $(\Delta R/R)_{\text{coinc}}$ changes linearly with I_{Pump} ²⁸. For (ii), $(\Delta R/R)_{\text{coinc}}$ was linearly corrected with $(1 - R(E_{\text{Pump}}))$ in b, where $R_{\text{Pump}}(E_{\text{Pump}})$ is the reflectivity of the pump at the pump frequency. Finally, in iii., we corrected $(\Delta R/R)_{\text{coinc}}$ linearly with I_{Pump} . The two largest corrections are by 80% ($E_{\text{Pump}} = 0.52$ eV) and 34% ($E_{\text{Pump}} = 0.56$ eV), but otherwise the corrections are less than 20%.

In figure 7 we observe an increasing $-(\Delta R/R)_{\text{coinc}}$ with increasing E_{Pump} up to 0.62 eV, then a decrease until 0.69 eV before a subsequent increase. With the analysis of the previous data (fig. 5), two important regimes can now be identified: for $E_{\text{Pump}} < 0.69$ eV ($E_{\text{Total}} < 1.82$ eV), $(\Delta R/R)_{\text{coinc}}$ is mostly governed by dispersion. For $E_{\text{Pump}} > 0.69$ eV, $(\Delta R/R)_{\text{coinc}}$ increases again due to a combination of both dispersive (n_2) as well as absorptive parts (β_{12}).

In the same figure 7, the differential reflectivity expected from the extended SWA is also plotted. Because this different reflectivity spectrum was obtained on domain A1, we first have to apply the SWA to the linear reflectivity from A1 (not shown). We obtain best agreement for $G = 2\pi/(363 \text{ nm})$ and $U_G = -1.2$. From the theoretical relation for a degenerate n_2 of a direct bandgap semiconductor⁴¹, $(\Delta R/R)_{\text{coinc}}$ is readily obtained. We note that a nondegenerate theory for indirect bandgap semiconductors is not available. We therefore have to interpret the measurements with respect to the theoretical relation cautiously. For $E_{\text{Pump}} < 0.7$ eV, the shape of the theoretical relation agrees excellently to our measurements. A strong divergence from the data is found for $E_{\text{Pump}} > 0.7$ eV, or $E_{\text{Total}} > 1.83$ eV. We interpret this threshold frequency marking a transition from dispersive behavior of $(\Delta R/R)_{\text{coinc}}$ to an absorptive behavior.

To verify the consistency of the time- and frequency resolved $\Delta R/R)_{\text{coinc}}$ taken on domain D4 (see section V A) with the pump frequency resolved $\Delta R/R)_{\text{coinc}}$ taken on domain A1, both n_2 and β_{12} (figure 5) were inserted into the SWA at A1, and plotted in figure 7. Good agreement to the measured differential reflectivity is found, from which we conclude that the extended SWA provides consistent description of our various data, measured at different pump intensities and on different sample domains.

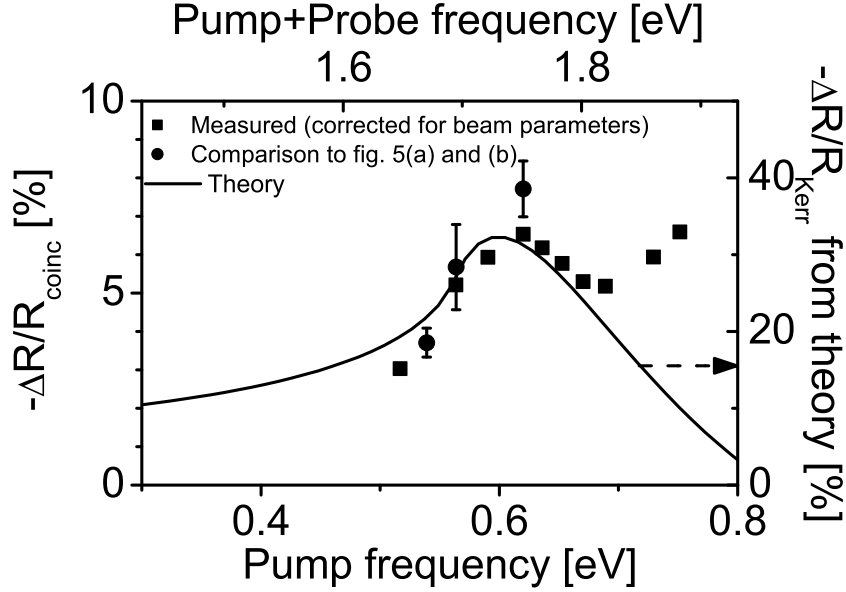


FIG. 7: Differential reflectivity at coincidence (squares, left scale) vs. pump frequency extracted from figure 3 and corrected for pump beam parameters. We have calculated the differential reflectivity expected from a nonlinear, purely dispersive direct bandgap material (curve)⁴¹ by inserting the theoretical relation for n_2 into the SWA. We can clearly see the 'purely dispersive assumption' is wrong for pump frequencies above $E_{\text{Pump}} = 0.69$ eV, or $E_{\text{Total}} = 1.82$ eV. Additionally, we have extracted complex values of n (from figure 5) and are plotted as circles. Good agreement to the measurements (squares) is found.

VI. NONDEGENERATE NONLINEAR FIGURE OF MERIT FOR FS SWITCHING

To quantify how useable a material is for optical switching, it is instructive to consider a figure of merit (FOM). Previously, Garmire proposed a degenerate FOM, a measure which indicates the maximum achievable phase shift of $2\pi \times \text{FOM}$, given that the device length is equal to the pump homogeneity length⁴⁴. The absolute length of the device then depends on the intensity used. From this requirement it follows that,

$$\text{FOM}(E_{\text{Pump}}) = n_2 / \lambda_{\text{Pump}} \beta_{11}, \quad (6)$$

where λ_{Pump} is the pump wavelength. A high FOM then is tantamount to a large phase shift, desirable for switching applications. Here we extend this notion to the general case by including nondegenerate absorption. Not only is the pump absorbed because it excites free carriers, but the probe is absorbed in the presence of the pump. The nondegenerate FOM (NFOM) is then⁵⁰

$$\text{NFOM}(E_{\text{Pump}}, E_{\text{Probe}}) = \frac{n_2(E_{\text{Pump}})}{\lambda_{\text{Pump}}\beta_{11}(E_{\text{Pump}}) + \lambda_{\text{Probe}}\beta_{12}(E_{\text{Pump}}, E_{\text{Probe}})}. \quad (7)$$

The NFOM has been calculated from our measured data as follows: $n_2(E_{\text{Pump}})$ has been derived from figure 5(b), where we have used the functional form of $n_2(E_{\text{Pump}})$ from⁴¹, but scaled it by a constant factor to match the magnitude of our data. An analytic form of β_{12} was derived by fitting an exponential to linear absorption coefficient $\alpha(E_{\text{Pump}} + E_{\text{Probe}})$. The exponential behavior of the linear absorption coefficient α with E_{Probe} close to the gap region is well documented⁴⁵. From $\alpha(E_{\text{Pump}} + E_{\text{Probe}})$, we deduce $\beta_{12} = \alpha(E_{\text{Pump}} + E_{\text{Probe}})/(2I_{\text{Pump}})$ from equation 3. Finally, an analytic expression for $\beta_{11}(E_{\text{Pump}})$ is obtained from the theoretical relation for $\beta_{11}(E_{\text{Pump}})$ for direct bandgap semiconductors from⁴¹, but again scaled by a factor to match our measurements (fig. 6).

Figure 8 shows the NFOM for different E_{Pump} and E_{Probe} . At summed frequencies $E_{\text{Total}} = E_{\text{Pump}} + E_{\text{Probe}}$, below the optical gap silicon ($E_{\text{Total}} < E_{\text{Opt}}$), the nondegenerate two-photon absorption is small, tantamount to a long probe absorption length, which is desired. If in addition $E_{\text{Pump}} < \frac{1}{2}E_G$, the pump absorption length becomes infinite. Higher order photon absorption has to be considered to give a quantitative estimate of the NFOM in this region of parameter space. Around $E_{\text{Pump}} = 0.8$ eV, n_2 crosses the abscissa and the NFOM approaches 0. For all other frequencies, NFOM depends strongly on both pump and probe frequencies. To achieve a high NFOM, it is advisable for E_{Total} to remain below the electronic bandgap, while E_{Pump} should remain just under $\frac{1}{2}E_G$. In that case, n_2 is high, while both β_{11} and β_{12} are kept low. We have indicated this line of maximum NFOM in fig. 8. These experimental conditions were recently realized by Hartsuiker *et al.* on a GaAs/AlAs microcavity⁴⁶. Our measurements have taken place in the parameter space indicated by the box. In this region, we find NFOM between 6×10^{-4} for $E_{\text{Probe}} = 1.24$ eV and $E_{\text{Pump}} = 0.75$ eV, and NFOM = 0.05 for $E_{\text{Probe}} = 1.09$ eV and $E_{\text{Probe}} = 0.58$ eV. The only other measurement of n_2 on a Si based photonic structure is¹⁹. We conclude that for a judicious choice of pump and probe frequency, the NFOM can be maximized by limiting both pump and nondegenerate probe

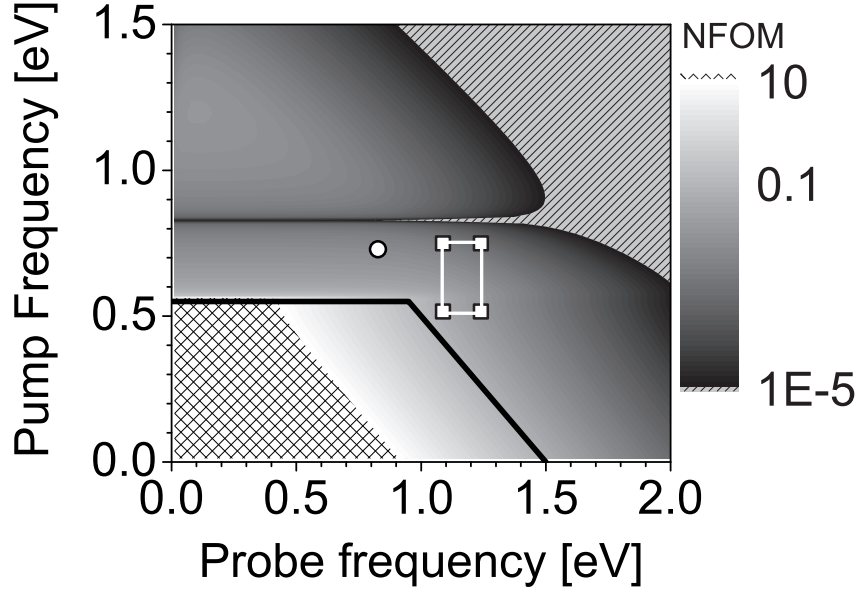


FIG. 8: nondegenerate Figure of Merit (NFOM) for instantaneous switching vs. pump and probe frequency for silicon (see eq. 7). For $E_{\text{Pump}} < \frac{1}{2}E_G$ ($=0.56$ eV), pump absorption is absent as we do not consider higher order photon absorption. If in addition $E_{\text{Pump}} + E_{\text{Probe}} < E_{\text{Opt}}$, the total absorption is 0 leading to large NFOM outside of the scale of graph (crossed area). Cross-sections of higher order photon absorption are required to calculate the NFOM at these pump and probe frequencies. The black curve indicates the parameter space for which a maximum NFOM is reached. At $E_{\text{Pump}} = 0.8$ eV, the region where $n_2(E_{\text{Pump}})$ tends to $0 \text{ cm}^2\text{GW}^{-1}$, and so the NFOM vanishes. For $E_{\text{Total}} \gg E_{\text{Opt}}$, the NFOM is $< 1 \times 10^{-5}$ (hatched area). The parameter space from our measurements are bounded by the box (squares), the only other measurement of n_2 on a Si based photonic structure is¹⁹ (circle).

absorption.

VII. CONCLUSION AND RECOMMENDATIONS

We have switched a silicon woodpile photonic crystal optically by both Kerr nonlinearities as well as optical free carrier injection. For the former we obtain changes in the real part of

the refractive index of up to 1×10^{-3} , and simultaneous changes in the imaginary part of 4×10^{-3} , together leading to a change in reflectivity of 1%. Free carriers caused refractive index changes of up to 3.5×10^{-3} and concomitant changes in reflectivity of up to $\Delta R = 2.5\%$. At pump-probe coincidence ($\Delta t < 100$ fs), we find that for $E_{\text{Total}} < 1.8$ eV, the reflectivity changes are due to the Kerr nonlinearity. In this case, the probe absorption length is limited by the pump power. For $E_{\text{Total}} > 1.8$ eV, the reflectivity starts to be dominated by pump-assisted absorption. For lower E_{Total} , it seems feasible to switch via the Kerr effect. Spontaneously emitted photons from an emitter placed inside the crystal are then not absorbed. We have extended the figure of merit for Kerr switching to include nondegenerate two-photon absorption. For Ti-Sapph lasers used in several previous experiments, ($E_{\text{Pump}} = 1.55$ eV), the NFOM is forbiddingly small.

In spite of the difficulties in analyzing nondegenerate optical properties of a photonic bandgap crystal, we have measured a clear difference in response of $E_{\text{Total}} < E_{\text{Opt}}$ and $E_{\text{Total}} > E_{\text{Opt}}$. This difference has ramifications on future experiments on nondegenerate instantaneous switching photonic bandgap crystals. DOS switching, and ultimately spontaneous emission switching is limited by the magnitude of pump and emission frequencies.

To exploit Kerr switching, that is to maximize NFOM, following improvements are proposed. In first instance it seems useful to pump and probe with the same polarization. For collinear polarization, a factor 3 improvement is predicted with respect to orthogonal polarization⁴⁷. Furthermore, the optical properties of the photonic crystal could be so tailored as to enhance the field. Calculations by us on a 1D Distributed Bragg Reflector have revealed that the field can significantly be enhanced when pumping at either the red or blue stopband edge, while the position of the field maximum depends critically on the exact pump frequency.

While a high-bandgap semiconductor will be less prone to nondegenerate absorption, n_2 scales with E_G^{-3} . The absorption can also be diminished by a lower pump intensity, which also goes at the expense of $\Delta n = n_2 I_{\text{Pump}}$. We therefore conclude that many obstacles will have to be overcome before Kerr switching can usefully be exploited.

VIII. ACKNOWLEDGEMENTS

We thank Henry van Driel and Allard Mosk for discussions. This work is part of the research program of the "Stichting voor Fundamenteel Onderzoek der Materie (FOM)", which was supported by the "Nederlandse Organisatie voor Wetenschappelijk Onderzoek (NWO)".

-
- ¹ P. M. Johnson, A. F. Koenderink, and W. L. Vos, "Ultrafast switching of photonic density of states in photonic crystals," *Phys. Rev. B* **66**, 081102(R) (2002).
 - ² B. P. J. Bret, T. L. Sonnemans, and T. W. Hijmans, "Capturing a light pulse in a short high-finesse cavity," *Phys. Rev. A* **68**, 023807 (2003).
 - ³ V. R. Almeida, C. A. Barrios, R. R. Panepucci, and M. Lipson, "All-optical control of light on a silicon chip," *Nature (London)* **431**, 1081 – 1084 (2004).
 - ⁴ Q. Xu, V. R. Almeida, and M. Lipson, "Micrometer-scale all-optical wavelength converter on silicon," *Opt. Lett.* **30**, 2733–2735 (2005).
 - ⁵ S. F. Preble, Q. Xu, and M. Lipson, "Changing the colour of light in a silicon resonator," *Nat. Phot.* **1**, 293–296 (2007).
 - ⁶ P. J. Harding, T. G. Euser, Y. R. Nowicki-Bringuier, J.-M. Gérard, and W. L. Vos, "Ultrafast optical switching of planar GaAs/AlAs photonic microcavities," *Appl. Phys. Lett.* **91**, 111103 (2007).
 - ⁷ X. Hu, P. Jiang, C. Ding, H. Yang, and Q. Gong, "Picosecond and low-power all-optical switching based on an organic photonic-bandgap microcavity," *Nat. Phot.* **2**, 185–189 (2008).
 - ⁸ A. Chin, K. Y. Lee, B. C. Lin, and S. Horng, "Picosecond photoresponse of carriers in Si ion-implanted Si," *Appl. Phys. Lett.* **69**, 653655 (1996).
 - ⁹ M. Först, J. Niehusmann, T. Plötzing, J. Bolten, T. Wahlbrink, C. Moormann, and H. Kurz, "High-speed all-optical switching in ion-implanted silicon-on-insulator microring resonators," *Opt. Lett.* **32**, 2046–2048 (2007).
 - ¹⁰ T. Tanabe, K. Nishiguchi, A. Shinya, E. Kuramochi, H. Inokawa, and M. Notomi, "Fast all-optical switching using ion-implanted silicon photonic crystal nanocavities," *Opt. Lett.* **90**, 031115 (2007).

- ¹¹ K. Yoshino, Y. Shimoda, Y. Kawagishi, K. Nakayama, and M. Ozaki, “Temperature tuning of the stop band in transmission spectra of liquid-crystal infiltrated synthetic opal as tunable photonic crystal,” *Appl. Phys. Lett.* **75**, 932–934 (1999).
- ¹² K. Busch and S. John, “Liquid-crystal photonic-band-gap materials: The tunable electromagnetic vacuum,” *Phys. Rev. Lett.* **83**, 967–970 (1999).
- ¹³ S. W. Leonard, J. P. Mondia, H. M. van Driel, O. Toader, S. John, K. Busch, A. Birner, U. Gösele, and V. Lehmann, “Tunable two-dimensional photonic crystals using liquid-crystal infiltration,” *Phys. Rev. B* **61**, 2389–2392 (2000).
- ¹⁴ I. Fushman, E. Waks, D. Englund, N. Stoltz, P. Petroff, and J. Vučković, “Ultrafast nonlinear optical tuning of photonic crystal cavities,” *Appl. Phys. Lett.* **90**, 091118 (2007).
- ¹⁵ M. Notomi and S. Mitsugi, “Wavelength conversion via dynamic refractive index tuning of a cavity,” *Phys. Rev. A* **73**, 051803 (2006).
- ¹⁶ M. Dinu, F. Quochi, and H. Garcia, “Third-order nonlinearities in silicon at telecom wavelengths,” *Appl. Phys. Lett.* **82**, 2954–2956 (2003).
- ¹⁷ A. D. Bristow, N. Rotenberg, and H. M. van Driel, “Two-photon absorption and Kerr coefficients of silicon for 850–2200 nm,” *Appl. Phys. Lett.* **90**, 191104 (2007).
- ¹⁸ Q. Lin, J. Zhang, G. Piredda, R. W. Boyd, P. M. Fauchet, and G. P. Agrawal, “Dispersion of silicon nonlinearities in the near infrared region,” *Appl. Phys. Lett.* **91**, 021111 (2007).
- ¹⁹ A. Haché and M. Bourgeois, “Ultrafast all-optical switching in a silicon-based photonic crystal,” *Appl. Phys. Lett.* **77**, 4089–4091 (2000).
- ²⁰ D. A. Mazurenko, R. Kerst, J. I. Dijkhuis, A. V. Akimov, V. G. Golubev, D. A. Kurdyukov, A. B. Pevtsov, and A. V. Sel’kin, “Ultrafast optical switching in three-dimensional photonic crystals,” *Phys. Rev. Lett.* **91**, 213903 (2003).
- ²¹ S. R. Hastings, M. J. A. de Dood, H. Kim, W. Marshall, H. S. Eisenberg, and D. Bouwmeester, “Ultrafast optical response of a high-reflectivity GaAs/AlAs Bragg mirror,” *Appl. Phys. Lett.* **86**, 031109 (2005).
- ²² T. G. Euser, A. J. Molenaar, J. G. Fleming, B. Gralak, A. Polman, and W. L. Vos, “All-optical ultrafast switching of Si woodpile photonic band gap crystals,” *arXiv:physics/0603045* (2006).
- ²³ T. G. Euser, A. J. Molenaar, J. G. Fleming, B. Gralak, A. Polman, and W. L. Vos, “All-optical ultrafast switching of Si woodpile photonic band gap crystals,” *Phys. Rev. B* **77**, 115214 (2008).
- ²⁴ M. Sheik-Bahae, A. A. Said, T. H. Wei, D. J. Gahan, and E. W. van Stryland, “Sensitive

- measurement of optical nonlinearities using a single beam,” IEEE J. Quantum Electron. **26**, 760 (1991).
- ²⁵ T. G. Euser, “Ultrafast optical switching of photonic crystals,” Ph.D. thesis, University of Twente (2007).
- ²⁶ J. G. Fleming and S. Lin, “Three-dimensional photonic crystal with a stop band from 1.35 to $1.95\mu\text{m}$,” Opt. Lett. **24**, 49–51 (1999).
- ²⁷ K. M. Ho, C. T. Chan, and C. M. Soukoulis, “Existence of a photonic gap in periodic dielectric structures,” Phys. Rev. Lett. **65**, 3152–3155 (1990).
- ²⁸ A. J. Molenaar, “Ultrafast optical switching of woodpile photonic crystals,” Master’s thesis, Complex Photonic Systems, Universiteit Twente (2006).
- ²⁹ B. Gralak, M. J. A. de Dood, G. Tayeb, S. Enoch, and D. Maystre, “Theoretical study of photonic band gaps in woodpile crystals,” Phys. Rev. E **67**, 066601 (2003).
- ³⁰ K. M. Ho, C. T. Chan, C. M. Soukoulis, R. Biswas, and M. Sigalas, “Photonic band gaps in three dimensions: New layer-by-layer periodic structures,” Sol. St. Commun. **89**, 413–416 (1994).
- ³¹ W. L. Vos, H. M. van Driel, M. Megens, A. F. Koenderink, and A. Imhof, *Experimental probes of the optical properties of photonic crystals*, Proceedings of the NATO ASI “Photonic Crystals and Light Localization in the 21st century” (Kluwer, Dordrecht, 2001).
- ³² A. F. Koenderink, “Emission and transport of light in photonic crystals,” Ph.D. thesis, University of Amsterdam (2003).
- ³³ M. J. A. de Dood, B. Gralak, A. Polman, and J. G. Fleming, “Superstructure and finite-size effects in a Si photonic woodpile crystal,” Phys. Rev. B **67**, 035322 (2003).
- ³⁴ T. G. Euser and W. L. Vos, “Spatial homogeneity of optically switched semiconductor photonic crystals and of bulk semiconductors,” J. Appl. Phys. **97**, 043102 (2005).
- ³⁵ J. F. Reintjes and J. C. McGroddy, “Indirect two-photon transitions in Si at $1.06\mu\text{m}$,” Phys. Rev. Lett. **30**, 901–903 (1973).
- ³⁶ H. K. Tsang, C. S. Wong, T. K. Liang, I. E. Day, S. W. Roberts, A. Harpin, J. Drake, and M. Asghari, “Optical dispersion, two-photon absorption and self-phase modulation in silicon waveguides at $1.5\mu\text{m}$ wavelength,” Appl. Phys. Lett. **80**, 416–418 (2002).
- ³⁷ J. A. Woollam Co., Inc., *Variable Angle Spectroscopic Ellipsometry Handbook (WVASE32)* (1987).

- ³⁸ C. Rotaru, S. Nastase, and N. Tomozeiu, “Amorphous phase influence on the optical bandgap of polysilicon,” *Phys. Stat. Sol. (a)* **171**, 365–370 (1999).
- ³⁹ H. Garcia and R. Kalyanaraman, “Phonon-assisted two-photon absorption in the presence of a dc-field: the nonlinear Franz-Keldysh effect in indirect gap semiconductors,” *J. Phys. B* **39**, 2737–2746 (2006).
- ⁴⁰ D. C. Hutchins and E. W. V. Stryland, “Nondegenerate two-photon absorption in zinc blende semiconductors,” *J. Opt. Soc. Am. B* **9**, 2065–2074 (1992).
- ⁴¹ M. Sheik-Bahae, D. J. Hagan, and E. W. V. Stryland, “Dispersion and band-gap scaling of the electronic Kerr effect in solids associated with two-photon absorption,” *Phys. Rev. Lett.* **65**, 96–99 (1991).
- ⁴² K. Sokolowski-Tinten and D. von der Linde, “Generation of dense electron-hole plasmas in silicon,” *Phys. Rev. B* **61**, 2643–2650 (2000).
- ⁴³ K. Ikeda, Y. Shen, and Y. Fainman, “Enhanced optical nonlinearity in amorphous silicon and its application to waveguide devices,” *Opt. Express* **15**, 17761–17771 (2007).
- ⁴⁴ E. Garmire, “Nonlinear optics in semiconductors,” *Phys. Today* **47**, 42–48 (1994).
- ⁴⁵ C. Klingshirn, *Semiconductor Optics* (Springer, 2005).
- ⁴⁶ A. Hartsuiker, P. J. Harding, Y.-R. Nowicki-Bringuier, J.-M. Gérard, and W. L. Vos, “Kerr and free-carrier ultrafast all-optical switching of GaAs/AlAs nanostructures near the three-photon edge of GaAs,” *arXiv:0806.3184v1* (2008).
- ⁴⁷ M. Sheik-Bahae, J. Wang, and E. W. V. Stryland, “Nondegenerate optical Kerr effect in semiconductors,” *IEEE J. Quantum Electron.* **30**, 249–255 (1994).
- ⁴⁸ Indeed, this Kerr nonlinearity was also claimed by our group²², but was later corrected in the final version²³.
- ⁴⁹ We had independently measured the radius of the beam waist at the focus, and had confirmed that the radius is diffraction limited.
- ⁵⁰ We note that the n_2 in equation 7 depends on E_{Pump} only. Measurements of nondegenerate n_2 are still outstanding in literature.